Development of an anisotropic pressure fluctuation model for the prediction of turbulence-induced vibrations of fuel rods

Zwijsen, K.; van den Bos, N.; Frederix, E. M.A.; Roelofs, F.; van Zuijlen, A. H.

DOI
10.1016/j.nucengdes.2024.113316

Publication date
2024

Document Version
Final published version

Published in
Nuclear Engineering and Design

Nuclear Engineering and Design 425 (2024) 113316

Contents lists available at ScienceDirect

Nuclear Engineering and Design

journal homepage: www.elsevier.com/locate/nucengdes

Development of an anisotropic pressure fluctuation model for the prediction of turbulence-induced vibrations of fuel rods

K. Zwijsen [a,*], N. van den Bos [a], E.M.A. Frederix [a], F. Roelofs [a], A.H. van Zuijlen [b]

[a] Nuclear Research and Consultancy Group (NRG), Westerduinweg 3, 1755 LE Petten, the Netherlands
[b] Faculty of Aerospace Engineering, Delft University of Technology, Kluyverweg 1, 2629 HS Delft, the Netherlands

ARTICLE INFO

Keywords:
Flow Induced Vibration
Fluid Structure Interaction
URANS
Synthetic Turbulence
Fuel Rods

ABSTRACT

The vibration of fuel rods induced by the fast flowing coolant is a known challenge to nuclear power plant designers and operators. If not dealt with adequately, the vibrations could lead to undesirable wear and tear of the cladding, which, in turn, could result in fuel rod failures and costly unplanned outages of the power plant. Hence, knowledge of these vibrations is important in the design phase. Due to the increase in computational power, numerical tools are increasingly often used to assess flow-induced vibrations. As these vibrations are a result of the local axial turbulent flow, scale-resolving methods are typically required for accurate predictions. Such methods, though, are usually computationally too expensive to use for industrial nuclear applications. Medium resolution turbulence models such as URANS generally cannot be used as they only resolve the average flow conditions and not turbulent fluctuations. To overcome this limitation of the URANS models, an Anisotropic Pressure Fluctuation Model (AniPFM) has been developed, which is an improved version of the earlier developed isotropic version. Compared to the isotropic model the generated synthetic turbulence is now anisotropic and is correlated in time based on the transport and decorrelation of turbulence. The current paper gives an overview of the new AniPFM, and presents results for a first fluid–structure interaction test case, demonstrating it can indeed induce and sustain vibrations of a rod, and that results are improved compared to the old model.

1. Introduction

In nuclear power plants, Flow-Induced Vibration (FIV) may cause fatigue problems, stress corrosion cracking, possible failure modes and fretting wear (Luk, 1993). This may eventually lead to nuclear safety issues and substantial standstill costs due to unplanned outage or even to the shutdown of a complete nuclear power unit, e.g., the San Onofre Nuclear Generation Station (NRC, 2015). The increase in power density of nuclear plants often results in the increase of the coolant flow. This may alter the flow and structural behavior, and cause flow-induced vibrations to become more prominent (Weaver et al., 2000). It is, therefore, important to assess this phenomenon early in the design process. Because of this, the field of FIV is becoming an increasingly important area of research.

A number of analytical models have been developed to model FIV. These models, though, are developed for simplistic cases, such as slender bodies in axial or cross flow (Lighthill, 1960). Also, due to the low-density ratio ($\rho_s/\rho_f < 10$) between the solid and fluid, a strong coupling between fluid and the in-core structural elements exists (Banks et al., 2014; Causin et al., 2005; Yang et al., 2008). Such cases are too complex to solve analytically. However, with the increase in computational power, it has become possible to simulate such scenarios.

Different parts of the nuclear reactor can vibrate due to entirely different FIV excitation mechanisms, and thus potentially require different numerical approaches to simulate them. Pettigrew et. al. (M. J., Pettigrew, C. E. Taylor, N. J. Fisher, M. Yetisir, and B.A.W. Smith, , 1998) created a classification of four FIV excitation mechanisms for different flow situations in nuclear reactor applications and their relative importance in various parts of a nuclear power plant. In areas of cross flow, Fluid Elastic Instability (FEI) and Periodic Wake Shedding (which causes Vortex-Induced Vibrations or VIV) are the main concerns for failure. Such cross flow is a predominant concern in the U-bend region of Steam Generators (SG), where FIV could potentially lead to Steam Generator Tube Rupture (SGTR) (Kotthoff, 1984; MacDonald et al., 1996). As the main driving mechanism behind VIV is periodic vortex shedding, this could potentially be predicted using an Unsteady Reynolds-Averaged Navier Stokes (URANS) approach (Hussain et al., 2022).

* Corresponding author.
E-mail address: zwijsen@nrg.eu (K. Zwijsen).

https://doi.org/10.1016/j.nucengdes.2024.113316
Received 13 March 2024; Received in revised form 14 May 2024; Accepted 14 May 2024
Available online 28 May 2024

Another area of concern in nuclear plants in the context of FIV is the reactor core. According to EPRI (Epri, 2008), over 70 % of all fuel rod leakages in US Pressurized Water Reactors (PWRs) is due to wear caused by flow-induced vibrations. In the fuel assemblies, the flow is in axial direction (parallel to fuel rods) and the driving FIV mechanism is Turbulence-Induced Vibrations (TIV), as the vibrations of the fuel rods are driven by the local, small-scale, turbulent velocity and pressure fluctuations. These fluctuations can numerically be resolved by, for example, the use of scale-resolving methods such as Large-Eddy Simulations (LES) or Direct Numerical Simulations (DNS). The drawback of these simulations though is that they require a large amount of computational power, and time, and hence cannot be applied to most industrial applications. Cheaper numerical tools, such as those based on the URANS approach, which are widely used in the industry, do not resolve the turbulent fluctuations causing the structural vibrations.

To overcome this, the Nuclear Research & consultancy Group (NRG) in the Netherlands has been working on the development of the Pressure Fluctuation Model (PFM) (Kottapalli et al., 2017; Kottapalli et al., 2019). This model makes use of local average velocity and turbulence fields to create instantaneous velocity fluctuations. With these velocity fluctuations, the pressure fluctuations can be calculated. These, in turn, are added to the averaged pressure and fed to the structural solver as boundary conditions. This combined URANS-PFM model has been tested in a selected number of FIV cases and from comparison to experimental data it was found that the PFM predicts vibration amplitudes in the same order of magnitude (Kottapalli et al., 2019). However, from the numerical tests it was also found that the PFM still has some shortcomings. One of the major shortcomings is that the spatial and temporal correlation of the produced turbulent velocity fluctuations is underpredicted, resulting in a significant underestimation of the Root-Mean Square (RMS) pressure fluctuations. A second shortcoming is that the PFM assumes isotropic turbulence. However, the vibrations in fuel rods subjected to axial flow are caused by the turbulence generated at the walls, which is anisotropic in nature.

To overcome these, an improved pressure fluctuation model, called AniPFM, has been created (van den Bos et al., 2022). The new model tackles among others the above-listed limiting assumptions of the PFM. First validation tests based on fluid flow simulations showed AniPFM can more accurately reproduce velocity and pressure fluctuation statistics than the old PFM. In this paper, results of a first FIV validation test are presented. In the next Section Chapter 2, the new AniPFM is described in detail. Subsequently, in Chapter 3, the numerical framework in which AniPFM is implemented and which is used to simulate flow-induced vibration is discussed. In Chapter 4, a first FIV test case is presented, with results compared to available experimental data, and to other available numerical results. Finally, in Chapter 5, conclusions and future work are listed.

2. Anisotropic pressure fluctuations model

In this chapter, the new AniPFM is discussed. The name is derived from the fact that this model is able to reproduce anisotropic Reynolds stresses. It is based on the formulation of the PFM as presented by Kottapalli et al. (Kottapalli et al., 2019), though major modifications have been made to incorporate anisotropy and accurate time correlation, using, amongst others, approaches from Billson et al. (Billson et al., 2004), and Shur et al. (Shur et al., 2014). First, the generation of velocity fluctuations is discussed, including the separate components and steps needed to create them. After this, the generation of the pressure fluctuations is discussed. Finally, the numerical framework in which the AniPFM is implemented and which is used to simulate FIV problems is presented.

2.1. Dimensionless velocity fluctuations

The first step in generating velocity fluctuations that are a function of space and time and with which an anisotropic turbulent velocity field can be reconstructed is to construct dimensionless velocity fluctuations that are solely a function of space. These dimensionless fluctuations $\boldsymbol{w}_t(x)$ are created by a Fourier decomposition as follows, similarly to what is done by Shur et al. (Shur et al., 2014):

$$\boldsymbol{w}_t(x) = \sqrt{6}\sum_n^N \sqrt{q_n}[\boldsymbol{\sigma}_n \cos(\boldsymbol{k}_n \bullet \boldsymbol{x} + \varphi_n)], \tag{1}$$

here, q_n is the mode amplitude, $\boldsymbol{\sigma}_n$ is the direction vector, $\boldsymbol{k}_n$ is the wavenumber vector, and φ_n is a random phase shift with a uniform distribution. The subscript n denotes the n-th Fourier mode, with in total N modes.

2.1.1. Wavenumber range

There are three important parts to create a proper Fourier decomposition of the dimensionless velocity fluctuations, viz. (a) the choice of the range and distribution of the N modes used, (b) the specification of the amplitude of each mode, which represents the energy contained in that mode, and (c) setting the direction of each mode. For the third part, it requires specifying a starting mode k_{start}, corresponding to the first mode, and an end mode k_{end}, which is mode N. The smallest wavenumber k_{start} corresponds to the largest eddy length scale L in the domain, for which a conservative estimate can be found from the following equation:

$$k_{start} = \frac{\epsilon}{\max(\|\boldsymbol{u}\|)}, \tag{2}$$

with ϵ the URANS energy dissipation rate and $\boldsymbol{u}$ the URANS velocity. Some other considerations must also be taken in account though in order to properly set k_{start}. First, the starting wavenumber must be lower than the wavenumber with the maximum energy density k_e. Furthermore, geometrical considerations must also be taken into account. For this, the user can input a user length scale l_{user}, which denotes the maximum length that can be captured given the geometry of the problem. For example, in turbulent channel flow the maximum wavelength in the wall-normal direction is equal to the channel height. Taken these considerations into account, the following expression is used for k_{start}:

$$k_{start} = \max\left[\min\left(k_{start}, \frac{1}{2}k_e\right), \frac{2\pi}{l_{user}}\right]. \tag{3}$$

As for k_{end}, a cut-off wavenumber is used

$$k_{end} = \frac{3}{2}k_{cut}, \tag{4}$$

with $k_{cut} = \frac{2\pi}{l_{cut}}$ and l_{cut} a user-defined cut-off length. Several expressions for this cut-off length were investigated, such as having it depend on the local cell size, as smaller waves would not be accurately resolved by the model. However, it was found that the cut-off length as defined by Shur et al. (Shur et al., 2014) gives the most accurate results:

$$l_{cut} = 2\min\left[\max\left(h_y, h_z, 0.3h_{max}\right) + 0.1d_w, h_{max}\right], \tag{5}$$

with h_y and h_z local cell sizes in spanwise and wall normal direction, respectively, h_{max} the maximum of the three local cell sizes, and d_w the distance to the wall. Given the wavenumber space from k_{start} to k_{end}, the space is divided in N intervals, with $N + 1$ edge wavenumbers. These edge-wavenumbers are used to define Δk_n. The edge-wavenumbers are logarithmically distributed.

2.1.2. Turbulent kinetic energy spectrum

The mode amplitude q_n specifies the amount of energy contained in that mode. Similarly to the old PFM, it is defined by a modified Von-Kármán energy spectrum $E(k)$. Though since for the AniPFM dimensionless velocity fluctuations are needed, the energy per mode is normalized in the following way:

$$q_n = \frac{E_k(k_n)\Delta k_n}{\sum_n^N E_k(k_n)\Delta k_n} \tag{6}$$

where $E_k(k_n)$ is the modified Von-Kármán energy spectrum evaluated at k_n. This spectrum is given by the expression:

$$E(k) = \frac{(k/k_e)^4}{\left[1+2.4\left((k/k_e)^2\right)\right]^{17/6}} \exp\left(-\left(12\frac{k}{k_\eta}\right)^2\right) f_{cut}, \tag{7}$$

where k_e is the earlier mentioned wavenumber at which the energy spectrum has its maximum, and k_η is the Kolmogorov wavenumber. This spectrum is very similar to the one used in the old PFM, however, a big difference is that now the constant A found in the previously used expression for the spectrum is no longer necessary, as the value for q_n is scaled by normalization. Because of this, the integral used to determine this constant A does not have to be evaluated, which reduces the total computational time and the complexity of the model. Note that the integral of the used energy spectrum over all the wavenumbers, i.e., the integral of Equation (7) over k, is equal to the local turbulent kinetic energy as obtained from the URANS simulation.

The modified Von Kármán spectrum is multiplied by a cut-off filter f_{cut}. Without this cut-off filter, the spectrum continues until the Kolmogorov wavenumber. However, typically the mesh cannot resolve wavenumbers that far; otherwise, it would be more favorable to perform a DNS. Since the input spectrum would not be fully resolved, an aliasing effect can be found in the reconstruction of the energy spectrum. To counteract this, a cut-off filter is used, which improves the reconstructed energy spectrum. The used expression in AniPFM for the cut-off filter is (Shur et al., 2014):

$$f_{cut} = \exp\left(-\left[\frac{4\max(k-0.9k_{cut},0)}{k_{cut}}\right]^3\right), \tag{8}$$

with k_{cut} as given in Section 2.1.1.

2.1.3. Direction vector

The final part needed for a proper Fourier decomposition of the dimensionless velocity fluctuations is the specification of the wavenumber vector and its direction vector. For the former, AniPFM uses the same definition as previously used in the old PFM, see also Fig. 1:

$$\boldsymbol{k}_n = k_n[\sin\theta_n\cos\psi_n, \sin\theta_n\sin\psi_n, \cos\theta_n], \tag{9}$$

where θ_n, ψ_n and φ_n are random variables with distributions given by:

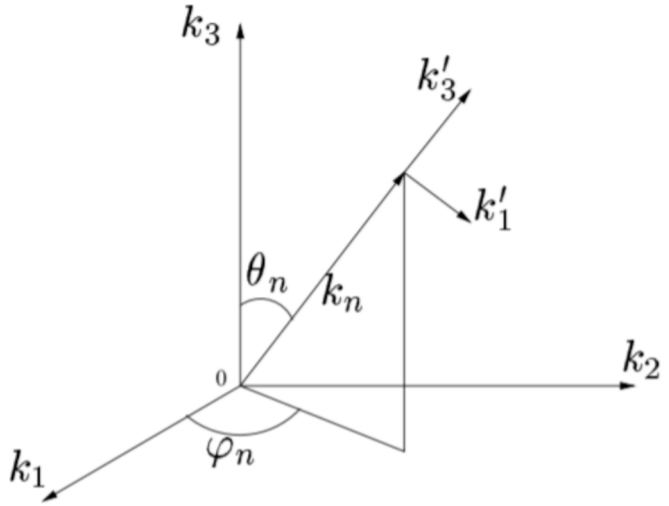

Fig. 1. Wave vector geometry of the n-th Fourier mode (Billson et al., 2004).

$$P(\psi_n) = \frac{1}{\pi}, P(\varphi_n) = \frac{1}{2\pi}, P(\theta_n) = \frac{1}{2}\sin(\theta_n). \tag{10}$$

The wavenumber direction vector is determined from the wavenumber vector. Based on continuity, it can be found that $\boldsymbol{k}_n \bullet \boldsymbol{\sigma}_n = 0$. To achieve this, $\boldsymbol{\sigma}_n$ is defined as the normalised cross-product between a random vector $\boldsymbol{\zeta}_n$, and the wavenumber vector:

$$\boldsymbol{\sigma}_n = \frac{\boldsymbol{\zeta}_n \times \boldsymbol{k}_n}{|\boldsymbol{\zeta}_n \times \boldsymbol{k}_n|}. \tag{11}$$

Since the dot-product of a vector with the cross product of the same vector is always equal to zero, the continuity condition is met.

2.2. Time correlation

The second step in generating the desired space–time dependent velocity fluctuations is implementing proper time correlation in the dimensionless and purely space-dependent velocity fluctuations of Section 2.1. Two phenomena contribute to the time correlation of the velocity field, namely the convection of the turbulent eddies and the decorrelation due to the production and dissipation terms. To introduce this time dependency, a two-step method similar to Billson et al. (Billson et al., 2004) is used:

$$\frac{\partial \boldsymbol{v}_t^{m-1}}{\partial t} + U_j\frac{\partial \boldsymbol{v}_t^{m-1}}{\partial x_j} = 0. \tag{12}$$

$$\boldsymbol{v}_t^m(\boldsymbol{x},t) = a\boldsymbol{v}_t^{m-1}(\boldsymbol{x}) + b\boldsymbol{w}_t^m(\boldsymbol{x}). \tag{13}$$

Here, $\boldsymbol{v}_t^{m-1}$ are the non-dimensional velocity fluctuations generated at time step *m-1*, and U_j is the Reynolds-averaged velocity as produced by URANS. In the first step, i.e. Eq. (12), the dimensionless velocity fluctuations are convected with the URANS velocity. Then, in the second step, a new solution $\boldsymbol{v}_t^m(\boldsymbol{x},t)$ is calculated from a combination of the (convected) previous solution $\boldsymbol{v}_t^{m-1}(\boldsymbol{x})$, and a newly generated field $\boldsymbol{w}_t^m(\boldsymbol{x})$. The coefficients a and b are defined by:

$$a = e^{-f_\tau \Delta t/\tau}, b = \sqrt{1-a^2}, \tag{14}$$

with τ the dissipation timescale determined from the URANS simulation, and f_τ a modification factor for fine-tuning the correlation. In line with (Billson et al., 2004), a value of $f_\tau = 17$ is used. Tests showed that this value gives a satisfactory correlation in the simulations of interest.

2.3. Scaling

The third and final step in generating velocity fluctuations is to scale the space–time dependent velocity fluctuations of Section 2.2 such that they replicate the desired Reynolds stresses and hence introduce the desired anisotropy. The final velocity fluctuations $\boldsymbol{u}_t(\boldsymbol{x},t)$ are constructed from non-dimensional isotropic fluctuations $\boldsymbol{v}_t(\boldsymbol{x},t)$ through the following expression:

$$\boldsymbol{u}_t(\boldsymbol{x},t) = a_{ij}\boldsymbol{v}_t(\boldsymbol{x},t), \tag{15}$$

With a_{ij} the Cholesky decomposition of the Reynolds stress tensor R, given by:

$$a_{ij} = \begin{bmatrix} \sqrt{R_{11}} & 0 & 0 \\ \frac{R_{21}}{a_{11}} & \sqrt{R_{22}-a_{21}^2} & 0 \\ \frac{R_{31}}{a_{11}} & \frac{(R_{32}-a_{31}a_{21})}{a_{22}} & \sqrt{R_{33}-a_{31}^2-a_{32}^2} \end{bmatrix}. \tag{16}$$

For the Cholesky decomposition a, it follows that $a^T a = R$. Thus, if $\langle$

$\boldsymbol{v}_t(\boldsymbol{x},t)^2\rangle = \delta_{ij}$, it follows that $\langle \boldsymbol{u}_t(\boldsymbol{x},t)^2\rangle$ is the Reynolds stress tensor. From this it can be concluded that $\boldsymbol{v}_t(\boldsymbol{x},t)$ must indeed be isotropic, and the squared-averaged components must be equal to unity.

With this method, the AniPFM can reconstruct anisotropic Reynolds stresses. For flows with a constant pressure gradient, such as channel flows, linear eddy viscosity models show isotropic Reynolds stresses. In order to improve the accuracy of these models, a correction is used to transform the isotropic tensor into an anisotropic tensor, based on the nonlinear eddy viscosity model of Wilcox (Wilcox, 1993):

$$\overline{u'u'} = \frac{8}{9}k, \overline{v'v'} = \frac{4}{9}k, \overline{w'w'} = \frac{6}{9}k. \tag{17}$$

2.4. Pressure fluctuations

With the three steps outlined in the previous sections, the desired space–time dependent velocity fluctuations are created. The velocity fluctuations require as input the turbulent kinetic energy and the turbulent dissipation rate. These are obtained from URANS. As the AniPFM must model the pressure fluctuations, it is necessary to derive how they relate to the generated velocity fluctuations. This dependence is derived in a similar way as done for the previous PFM.

First, in the incompressible momentum equation, the Reynolds decomposition of the velocity $\boldsymbol{u} = \overline{\boldsymbol{u}} + \boldsymbol{u}'$ and pressure $p = \overline{p} + p'$ is substituted. Then, the averaged momentum equation is subtracted, and the divergence operator is applied. This results in the following Poisson equation for the pressure fluctuations:

$$\frac{\partial^2 p'}{\partial x_i \partial x_i} = -\rho_f \left[2\frac{\partial \overline{u}_i}{\partial x_j}\frac{\partial u'_j}{\partial x_i} + \frac{\partial^2}{\partial x_i \partial x_j}\left(u'_i u_{j'} - \overline{u'_i u_{j'}}\right) \right]. \tag{18}$$

From this equation, it is evident that the pressure fluctuations only depend on the mean velocity $\overline{u_i}$ and the Reynolds stresses $\overline{u'_i u_{j'}}$, which can both be obtained from the URANS solution, and the modeled velocity fluctuations u'_i. Hence, all necessary ingredients are in place to generate the desired pressure fluctuations and to perform FIV simulations using URANS in combination with the Anisotropic Pressure Fluctuation Model.

2.5. Model overview

The previous sections outlined the necessary steps needed to generate the velocity fluctuations, and with those as input, the desired pressure fluctuations. In Fig. 2, the full model is summarized. First the non-dimensional velocity fluctuations are calculated, based on the energy spectrum. Then the time correlation is performed. After this, the velocity fluctuations are computed by scaling with the Cholesky tensor. Finally, p' can be computed.

3. Computational framework

AniPFM is implemented in the finite volume OpenFOAM framework, which is also used to solve for the governing fluid equations. The URANS equations are discretized in space with a PIMPLE algorithm which is a combination of the classical PISO and SIMPLE algorithms. The consistent second-order backward difference scheme (BDF2) developed for moving grids is used to integrate the equations in time. The mean pressure field resulting from the URANS solver is superimposed with the pressure fluctuations field coming out of AniPFM and subsequently passed on to the solid solver as boundary conditions.

The governing equations for the solid problem are solved by means of the finite element approach implemented in the library Deal.II (Alzetta, 2018). In particular, the linear finite element approximation is used to discretize the governing equations in space, and the Theta-method is used to integrate the structural equations in time. In all the cases reported in this work, the value $\theta = 0.6$ is used for the time

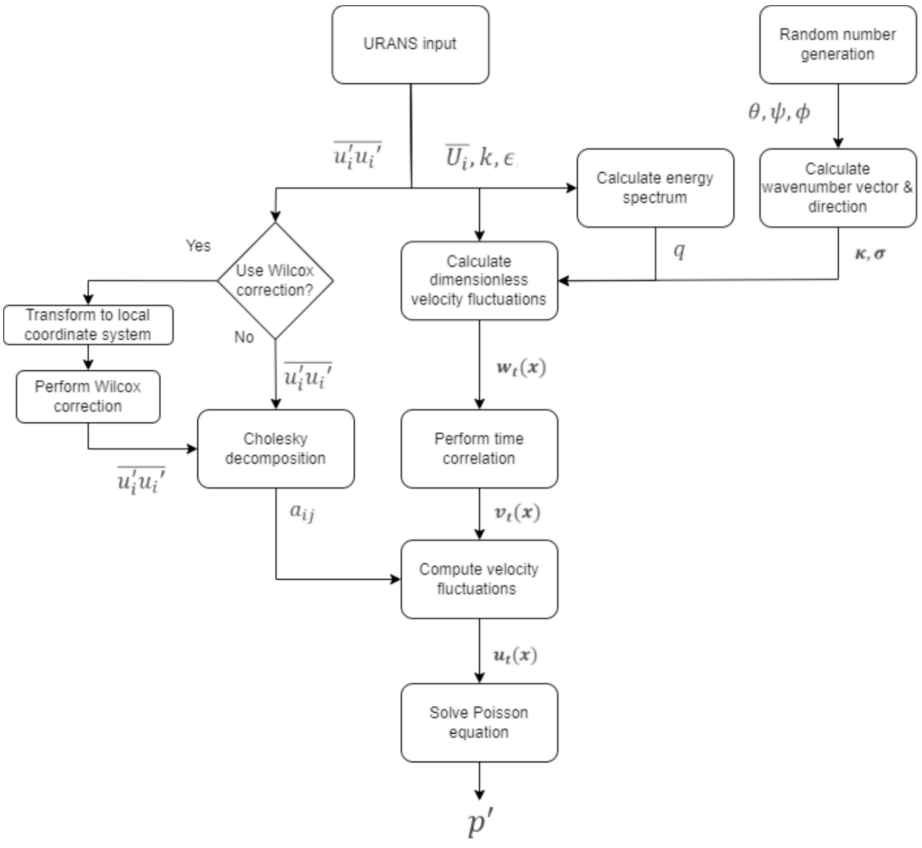

Fig. 2. A flow-chart of the different computational steps of the proposed AniPFM.

integration of the structural problem.

The fluid and solid solvers are coupled through the preCICE library (Bungartz, 2016) for solving Fluid-Structure Interaction (FSI) problems. Due to the fact that the fluid and solid meshes are generally not conformal at the fluid–structure interface, forces and displacements must be mapped from one grid to the other. To this purpose, radial basis functions implemented in preCICE are used to map the displacements from the solid to the fluid interface in a consistent way, and to map the forces from the fluid to the solid interface in a conservative way.

A partitioned, parallel implicit coupling solver is used to solve the FSI problem. In implicit approaches, the fluid flow and structural equations are solved iteratively until convergence of the FSI problem is achieved within one time step. Here, convergence means that the change in structural displacement as a result of the fluid load between subsequent iterations is below a certain tolerance. For all simulations reported here, the interface quasi-Newton technique with an approximation for the inverse of the Jacobian from a least-squares model (IQN-ILS) of (Degroote et al., 2009) is used as an acceleration technique for convergence. This method is proved to be more robust than Aitken's under-relaxation methods for strongly coupled problems.

4. Flexible brass beam in turbulent water

In (van den Bos et al., 2022), results of two fluid flow test cases that were performed to assess the performance of the AniPFM were presented. These two test cases were that of a homogeneous isotropic turbulent box, and of a turbulent channel flow. Velocity and pressure fluctuations statistics were compared to experimental data, and an improvement compared to the old PFM was found. A next step is to assess the performance of AniPFM in a test case involving FIV. To this end, the flexible brass beam experiment in turbulent water flow, performed by Chen & Wambsganss was selected (Chen and Wambsganss, 1972). This experiment was chosen because it closely mimics turbulence-induced vibrations found in nuclear reactors, and because it has been used in the past by other authors as a validation case for FSI problems with applications to nuclear fuel rods (Kottapalli et al., 2019; De Ridder et al., 2013; Nazari et al., 2019).

The current chapter first gives a short description of the experiment, followed by the setup used to perform the numerical simulations. Subsequently, results are presented, first of some pure fluid flow simulations with AniPFM, followed by AniPFM FSI simulations.

4.1. Experiment

The experiment consists of a flexible brass beam enclosed in a rigid steel cylinder, and that it is clamped on both sides. Water flows in the annular region between the brass beam and rigid cylinder, from the inlet to the outlet. The discretized geometry as used by Kottapalli et al. (Kottapalli et al., 2019) is shown in Fig. 3. The water is assumed isothermal and incompressible, with a density ρ_f equal to 1000 kg/m^3 and a kinematic viscosity $\nu_f = 1.0 \bullet 10^{-6} m^2/s$. The diameter of the brass beam is $D_c = 0.0127$ m, the enclosing cylinder has a diameter of $D_o = 0.0254$ m, and the beam has a length of L = 1.19 m. This gives an L/D-ratio of 93.7. The rod has a density of 8400 kg/m^3, giving a density ratio of $\rho_s/\rho_l = 8.4$. The experimental Poisson ratio was not reported, but a nominal value of 0.33 was taken, based on previous simulations (Kottapalli et al., 2019). Finally, a Young's modulus of E = 107 GPa was specified.

The level of turbulent intensity and the turbulent length scale at the inlet of the domain were not reported by (Chen and Wambsganss, 1972). Several studies (Kottapalli et al., 2019; De Ridder et al., 2013; Nazari et al., 2019) assumed a turbulence intensity of 5 % and a turbulent length scale of 0.1 cm. The experiment was conducted for various mean inlet velocities, in the range of 8–33 m/s. This gives a range of Reynolds numbers from 101,600–419,100. The experiment established both data about the modal frequencies for several flow cases, and the root-mean-squared vibration amplitudes.

4.2. Simulation setup

The configuration is set up such that the geometry and simulation closely match the experiment. For the simulations, a uniform inlet velocity is used, along with a turbulence intensity of 5 % and a turbulent length scale of 0.1 cm. From preliminary tests, it was determined that these values do not have a large effect on the results. The flow is fully developed for the majority (roughly 90 %) of the domain, and in this part, the kinetic energy profiles and pressure fluctuations are independent of the inlet conditions. Only near the inlet is a variation noticeable; however, the impact of this region on the structural vibration is hypothesized to be considerably less than that of the developed flow region of the domain.

The outer steel cylinder is kept rigid, whereas the inner brass beam is modelled as a moving wall. The brass beam is clamped at both ends, and it is assumed that the beam can be modelled with a linear elastic solver. For this, the relative displacements must be $A_{rms}/L \ll 1$, which can be found to be true based on the displacement values from the experiment. For the CFD side, URANS is used with the k − ω SST turbulence model.

The fluid flow simulations are resolved up to the wall, which means that fine grids are necessary. An example of a mesh is shown in Fig. 4, along with the used axis convention. Several fluid meshes are used to compare the results to the experiment and the simulations from previous papers. In these meshes, the axial and radial elements are varied to study its effects. The discretization in the tangential direction is fixed to 40 cells, which was found to be sufficient from a preliminary mesh study of pure CFD calculations. For the structural mesh, quadratic elements are

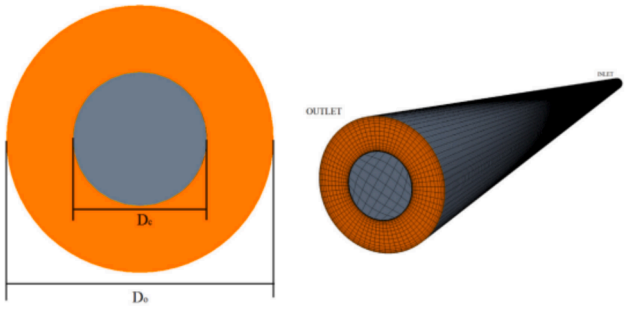

Fig. 3. Discretized geometry of Kottapalli et al. (Kottapalli et al., 2019), representing the experiment of Chen &Wambsganss (Chen and Wambsganss, 1972).

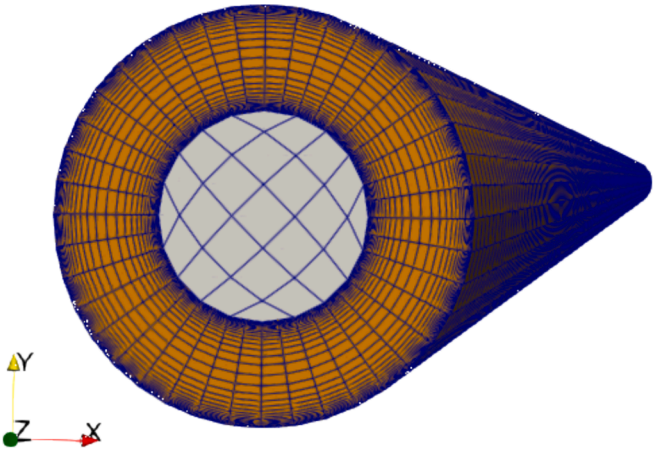

Fig. 4. Discretized geometry of the brass beam case.

used. From a preliminary mesh study, it was found that the results were converged for a structural mesh that has 25 elements in the x-y plane, and 50 elements in the axial direction, hence 1250 elements in total. For both the solid and the fluid models, a second-order time scheme is used.

4.3. URANS FSI simulation

Before performing the AniPFM FSI simulation, a free vibration FSI simulation is performed using pure URANS approach (without AniPFM). This simulation is performed with flowing water for an inlet velocity of 10 m/s. It serves as validation of the setup, i.e., whether the mapping method, the structural mesh and boundary conditions, and the coupling algorithm, are correct. For this calculation, the brass beam is subjected to an external load in a form of an initial distributed force for 0.015 s. This is the excitation mechanism, because with a pure URANS-approach, only the mean flow is resolved, without any pressure fluctuations responsible for inducing the vibrations.

The behaviour of an oscillating beam is known, and it can be represented with an exponentially damped sinusoid. In order to retrieve the natural frequency and the damping ratio, the displacements obtained from the FSI simulation are fitted to the function:

$$D(t) = A \bullet e^{-\lambda t} \bullet \cos(\omega t - \varphi) + \psi. \tag{19}$$

From this expression, the natural frequency f and damping ratio ζ can be obtained through:

$$f = \frac{2\pi}{\omega}, \zeta = \frac{\lambda}{\sqrt{\lambda^2 + \omega^2}}. \tag{20}$$

The displacement of the centre of the brass beam at z = 0.595 m is shown in Fig. 5. As can be seen, it indeed follows the exponentially damped sinusoid shape. The function shows to be an excellent fit, with the largest relative standard deviation of any fitting parameter being 0.044 %.

In Fig. 6, the fundamental natural frequency (left) and damping ratio (right) is compared with the experiment of Chen & Wambsganss (Chen and Wambsganss, 1972), as well as other simulations taken from literature (Kottapalli et al., 2019; De Ridder et al., 2013; Nazari et al., 2019). Note that from (De Ridder et al., 2013), the non-pre-stressed data is taken, in order to ensure a fair comparison. Furthermore, the experimental data from (Chen and Wambsganss, 1972) is denoted by the dots, whereas the line shows the theoretical results.

As can be seen from Fig. 6, the frequency is in close agreement with the experiments and the other simulations. There is an error of 5.7 % w.r.t. the analytical value, and an error of 5.4 % w.r.t. the closest experimental value. The results are comparable to other published results. As

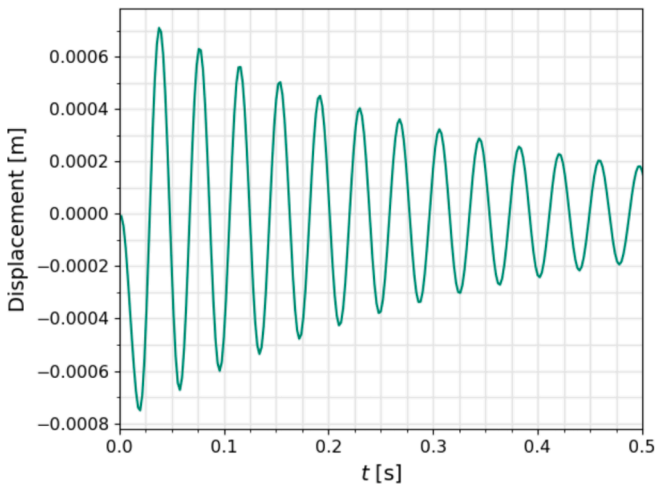

Fig. 5. The displacement at mid-beam, for 0.5 s of simulated time.

for the damping ratio, it was found that the results are similar to those of Kottapalli et al. (Kottapalli et al., 2019), but it shows a large error of 28.6 % with respect to the experiment of Chen & Wambsganss. It is believed that this is caused by the software packages used for the FIV simulations, as in other cases in which OpenFOAM – preCICE – Deal.II framework was used, also an overestimation in damping ratio compared with simulations done in STAR-CCM + was found (Chouchoulis, 2018).

4.4. AniPFM FSI simulation

From the previous results, it was found that the general FSI set-up is in line with previously published results and thus that the model setup can be used for FSI simulations involving AniPFM. In this section, the Root-Mean Square (RMS) amplitudes obtained using the AniPFM FSI simulation are compared to those of the experiment by Chen & Wambsganss (Chen and Wambsganss, 1972), in order to investigate the accuracy of the AniPFM. Simulations were performed for 10, 15, and 20 m/s fluid velocity. Note that not the same mesh is used in each simulation, but an equivalent mesh such that $y^+ = 1$ for all simulations is ensured. The maximum number of cells used in the simulations remains below the 1 M though.

The results for the various flow velocities are shown in Fig. 7. Here, again the dots indicate the experimental values of Chen & Wambsganss (Chen and Wambsganss, 1972), whereas the line indicates the values calculated by their analytical model. The error bars again note the 95 % confidence interval over the last 20 flow-through times. The results of the simulations using different initial seed numbers for generating random numbers are shown at 10 m/s. Although the effect of different seed numbers was not tested for higher velocities, the results at 10 m/s should give an indication of the uncertainty that can be assumed for higher flow velocities as well. Note that the results of Nazari et al. (Nazari et al., 2019) are not included, as they are one order of magnitude larger than all other data points.

The AniPFM shows a clear overestimation of the RMS amplitude, whereas the results of Kottapalli et al. (Kottapalli et al., 2019) and De Ridder et al. (De Ridder et al., 2013) show an underestimation. Note that the simulation performed by De Ridder is a pure LES simulation, not an FSI simulation. The RMS amplitude was obtained using the force frequency spectrum as input of the theoretical model of Chen & Wambsganss (Chen and Wambsganss, 1972). The results of Kottapalli et al. (Kottapalli et al., 2019) are obtained with a URANS FSI methodology combined with a pressure fluctuation model, similar to the method presented in this paper.

Looking at relative errors, AniPFM over-predicts the RMS displacement by about 30–40 %, which is similar in magnitude to that of De Ridder et al. (De Ridder et al., 2013). The relative error obtained by PFM is much larger though. Hence, from these first FIV simulations using AniPFM, it can be concluded that the use of the proposed AniPFM has shown an improvement in the prediction of the RMS amplitude, compared to the previous pressure fluctuation model proposed by Kottapalli et al. (Kottapalli et al., 2019). Although the AniPFM showed a similar error w.r.t. the RMS amplitude as the LES of De Ridder et al. at 10 m/s, due to lack of data at other mean flow velocities, no conclusions can be made about the general accuracy of the AniPFM versus LES. Applying AniPFM to further test cases should give a more detailed indication of the performance of AniPFM compared to other available numerical tools and methods for simulating turbulence-induced vibrations.

5. Conclusions

In this paper, a new anisotropic pressure fluctuation model, called AniPFM is described. This model allows for the prediction of turbulent pressure fluctuations when using a URANS approach, which can be useful in particular for turbulence-induced vibration prediction. Several aspects of the AniPFM were adjusted with respect to the previous PFM of

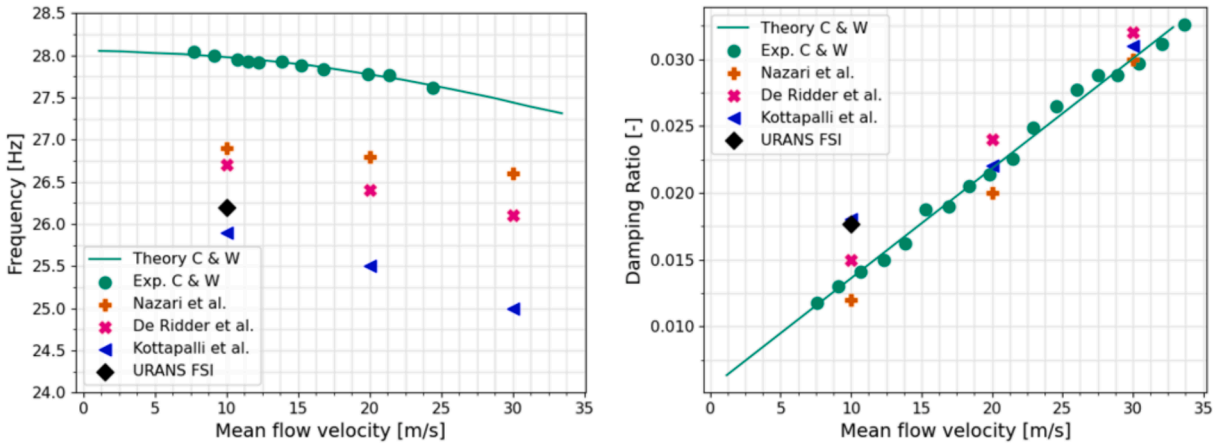

Fig. 6. The calculated frequencies (left) and damping ratios (right) of the current work, compared to various simulations as well as experimental results (Kottapalli et al., 2019; Chen and Wambsganss, 1972; De Ridder et al., 2013; Nazari et al., 2019).

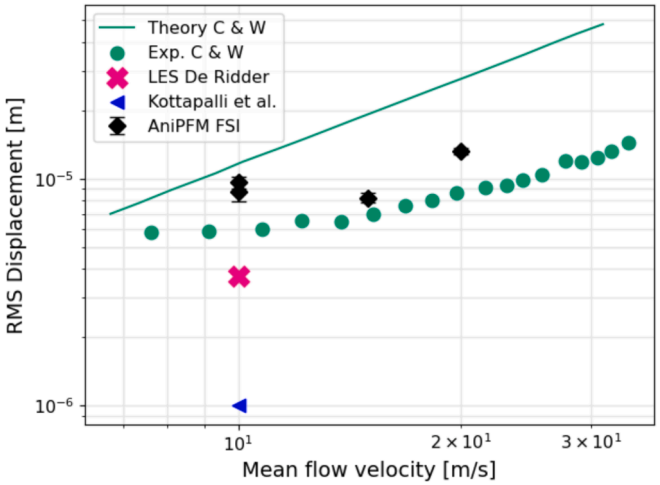

Fig. 7. The RMS vibration amplitudes of the brass beam of the current work, compared to various simulations as well as experimental results (Kottapalli et al., 2019; Chen and Wambsganss, 1972; De Ridder et al., 2013).

Kottapalli et al., namely the energy spectrum cut-off filter, the replication of anisotropic Reynolds stresses, and the method for time correlation.

In an earlier study, AniPFM was validated for pure flow-only cases, comparing velocity and pressure fluctuations statistics with available experimental data. As it showed satisfactory results, in this paper, a first application to an FIV test case is presented. This test case under consideration is that of a flexible brass beam subjected to axial turbulent water flow, as performed by Chen & Wambsganss in 1975. Results for URANS FSI simulations showed a good match for the natural frequency with the experimental one, though an over-prediction in the damping ratio. This latter is in line with what was observed previously with the numerical framework used. Next, results for FSI simulations involving AniPFM were compared with experimental data and other numerical results. Differences in RMS amplitudes of about 30–40 % were found, which is a significant improvement compared to the previous PFM.

Future work will be aimed at testing AniPFM on other test cases. Moreover, further development of the model is foreseen, such as the implementation of different energy spectra which can optionally be used for the individual velocity fluctuation component, such that true anisotropy can be accounted for in the model.

CRediT authorship contribution statement

K. Zwijsen: Writing – original draft, Validation, Supervision, Resources, Methodology, Investigation, Funding acquisition, Conceptualization. **N. van den Bos:** Methodology, Investigation, Conceptualization, Writing – review & editing. **E.M.A. Frederix:** Validation, Supervision, Methodology, Writing – review & editing. **F. Roelofs:** Writing – review & editing, Supervision, Project administration. **A. H. van Zuijlen:** Validation, Supervision, Methodology, Writing – review & editing.

Declaration of competing interest

The authors declare that they have no known competing financial interests or personal relationships that could have appeared to influence the work reported in this paper.

Data availability

No data was used for the research described in the article.

Acknowledgments

The authors would like to acknowledge the contribution of the GO-VIKING project (Grant Agreement No. 101060826) funded by the euratom research and training program 2022-2025 and that of the pioneer research program funded by the ministry of economic affairs at the nuclear research & consultancy group and the delft university of technology for supporting the research project and providing the necessary resources.

References

Alzetta, G., 2018. The deal.II library, version 9.0. J. Numer. Mathemat.
Banks, J.W., Henshawb, W.D., Schwendeman, D.W., 2014. An analysis of a new stable partitioned algorithm for FSI problems. Part I: Incompressible flow and elastic solids. J. Computat. Phys. 269 (2), 108–137.
M. Billson, L.-E. Eriksson and L. Davidson, "Jet Noise Modeling Using Synthetic Anisotropic Turbulence," in 10th AIAA/CEAS Aeroacoustics Conference, American Institute of Aeronautics and Astronautics (2004).
Bungartz, H.-J., et al., 2016. preCICE – a fully parallel library for multi-physics surface coupling. Comput. Fluids 141, 250–258.
Causin, P., Gerbeau, J.-F., Nobile, F., 2005. Added-mass effect in the design of partitioned algorithms for fluid-structure problems. Comput. Method. Appl. Mechan. Eng. 194 (42–44), 4506–4527.
Chen, S.S., Wambsganss, M.W., 1972. Parallel-flow-induced vibration of fuel rods. Nucl. Eng. Design 18 (2), 253–278.
J. Chouchoulis, "An advanced fluid-structure interaction software package for industrial problems in nuclear reactor applications", Master's thesis, TU Eindhoven (2018).

De Ridder, J., Degroote, J., Van Tichelen, K., Schuurmans, P., Vierendeels, J., 2013. Modal characteristics of a flexible cylinder in turbulent axial flow from numerical simulations. J. Fluid. Struct. 43, 110–123.

Degroote, J., Bathe, K., Vierendeels, J., 2009. Performance of a new partitioned procedure versus a monolithic procedure in fluid-structure interaction. Comput. Struct. 87 (11), 793–801.

EPRI, 2008, "Fuel Reliability Guidelines: PWR Grid-to-Rod Fretting", Technical report, 1015452. https://www.epri.com/research/products/1015452.

Hussain, M.M.M.D., Zwijsen, K., Roelofs, F., van Zuijlen, A.H., 2022. "URANS Simulations For Fluid-Structure Interaction Of Cylinders In Cross-Flow", NURETH-19. Belgium, Brussels.

Kottapalli, S., Sharma, S., Shams, A., Zuijlen, A.H., Pourquie, M.J.B.M., 2017. Numerical Simulation of Turbulence Induced Vibrations from URANS models using the Pressure Fluctuation Model. NURETH-17, Xi'an, China.

Kottapalli, S., Shams, A., van Zuijlen, A.H., Pourquie, M.J.B.M., 2019. Numerical investigation of an advanced U-RANS based pressure fluctuation model to simulate non-linear vibrations of nuclear fuel rods due to turbulent parallel-flow. Ann. Nucl. Energy 128.

K. Kotthoff, "Erkenntnisse aus dem Ablauf ausländischer Vorkommnisse mit Dampferzeuger-Heizrohrbruch", GRS, Technische Mitteilungen, Bd. 77, Nr. 1 (1984).

Lighthill, M., 1960. Note on the swimming of slender fish. J. Fluid Mechan. 9 (2), 305–316.

K. H. Luk, "Pressurized-Water Reactor Internals Aging Degradation Study," Oak Ridge National Laboratory (1993).

P. E. MacDonald, V. N. Shah, L. W. Ward, P. G. Ellison, "Steam Generator Tube Failures", NUREG/CR-6365 INEL-95/0383 (1996).

Nazari, T., Rabiee, A., Kazeminejad, H., 2019. Two-way fluid-structure interaction simulation for steady-state vibration of a slender rod using URANS and LES turbulence models. Nucl. Eng. Technol. 51 (2), 573–578.

NRC, https://www.nrc.gov/docs/ML1501/ ML15015A419.pdf (2015).

Pettigrew, M.J., Taylor, C.E., Fisher, N.J., Yetisir, M., Smith, B.A.W., 1998. Flow-induced vibration: recent findings and open questions. Nucl. Eng. Design 185 (2–3), 249–276.

Shur, M.L., Spalart, P.R., Strelets, M.K., Travin, A.K., 2014. Synthetic Turbulence Generators for RANS-LES Interfaces in Zonal Simulations of Aerodynamic and Aeroacoustic Problems. Flow, Turbul. Combust. 93 (5), 63–92.

van den Bos, N., Zwijsen, K., Van Zuijlen, A.H., Frederix, E.M.A., Roelofs, F., 2022. Turbulence-Induced Vibrations Prediction Through Use Of An Anisotropic Pressure Fluctuation Model. EPJ Nucl. Sci. Technol. accepted and in process.

D. Weaver, D. Weaver, S. Ziada, M. Au-Yang, Shoei-sheng Chen, M. Païdoussis, and M. Pettigrew, "Flow-Induced Vibrations in Power and Process Plant Components Progress and Prospects," *J. Press. Vessel Technol.*, **122**(3), pp. 339-348 (2000).

D.C. Wilcox, Turbulence modelling for CFD, DCW Industries (1993).

Yang, J., Preidikman, S., Balaras, E., 2008. A strongly coupled, embedded-boundary method for fluid structure interactions of elastically mounted rigid bodies. J. Fluid. Struct. 24 (2), 167–182.